Respiratory Physiology & Neurobiology 265 (2019) 40–48

Contents lists available at ScienceDirect

Respiratory Physiology & Neurobiology

journal homepage: www.elsevier.com/locate/resphysiol

Modeling hypoglossal motoneurons in the developing rat

Paul Allen Williams[a,b], Clarissa Dalton[c], Christopher G. Wilson[a,b,*]

[a] Division of Physiology, Basic Science Department, Loma Linda University School of Medicine, 11234 Anderson St., Loma Linda, CA 92350, USA
[b] Lawrence D. Longo, MD Center for Perinatal Biology, Loma Linda University School of Medicine 11234 Anderson St., Loma Linda, CA 92350, USA
[c] California Polytechnic State University, San Luis Obispo, CA, USA

ARTICLE INFO

Keywords:
Neonatal
Hypoglossal neurons
Morphology
Modeling
Electrophysiology

ABSTRACT

We hypothesize that developmental changes in motoneuron volume or surface area in the hypoglossal motor nucleus (XII) can alter the biophysical properties that contribute to motor output. We used the Golgi-Cox technique to stain developing hypoglossal motoneurons (XII MNs) at three postnatal ages (P3, 10, & 17). We removed Sprague-Dawley rat pup brains, processed, sectioned, stained, imaged, and performed 3D reconstructions to quantify the morphometrics of XII MNs. We then used the simulation environment, NEURON, to model the biophysical properties from digitally reconstructed neurons and compared our results to previously published experiments. The total volume of neurons increased from 4766 μm^3 for P3 to 16,904 μm^3 for P17 while the total surface area increased from 4258 μm^2 to 13,510 μm^2 respectively. The P3 simulations required a 10-fold reduction in the hyperpolarization-activated current and doubling of the membrane capacitance to match experimental results. XII MN morphology showed a direct relationship with passive electrophysiological properties and recapitulates the changes seen experimentally.

1. Introduction

Respiration is critical during development, throughout life, and must generate reliable, rhythmic motor output through an elaborate system of control. At birth, the autonomic regions in the brainstem, which generate and control respiratory rhythm, are not fully developed (Feldman et al., 2013; Feldman and Del Negro, 2006; Feldman and Smith, 1995). Normal control of breathing develops in the first few weeks after birth and the motoneurons (MNs) of the hypoglossal (XII) and other brainstem nuclei provide drive to the tongue and upper airways and are used in *in vitro* models to provide an index of fictive inspiratory effort (Feldman et al., 2013; Feldman and Del Negro, 2006). The critical role that tongue and upper airway control plays in speech is also an important aspect that motivates the study of XII MN development. We have previously shown that there are age-dependent changes in XII MN output drive, but the contribution of developmental changes in neural morphology remains essentially unknown (Fietkiewicz et al., 2011). Because the XII MNs are easy to identify and play an active role in inspiration during development, they are a convenient and accessible population of neurons for electrophysiological study. Also, since 80% or more of the neurons in the XII are MNs that are readily distinguishable from the interneurons, the XII MNs are convenient for morphological studies (Cooper, 1981; McClung and Goldberg, 1999).

Work by others has shown that development of the respiratory network plays a key role in changing breathing pattern (Liu et al., 2006; Mortola, 1984). Understanding the remodeling of the breathing neural network during early life is key to elucidating the synergy between changes in morphology and breathing rhythm in the perinatal period. It has been shown that neural network behavior is influenced by the morphology of neurons, and that connectivity is altered due to changes in neurotransmitter release as well as receptor up- and down-regulation (Ferrante et al., 2013; Komendantov and Ascoli, 2009). There is a body of work on the morphology and electrophysiology of motoneurons albeit only some work on XII MNs and a few studies on morphological changes during postnatal development (Carrascal et al., 2005; Kanjhan et al., 2016; Lindsey et al., 2012; Nunez-Abades and Cameron, 1995). Morphological differences in XII MNs have been shown between neonatal and adults as well as corresponding electrophysiological changes (Berger et al., 1996; Carrascal et al., 2005). It has also been demonstrated that the morphology and electrophysiology of motoneurons differ for various regions in the central nervous system (Carrascal et al., 2005). Although most electrophysiological changes in motoneurons have been attributed to changes or differences in the type, sub-type, and distributions of ion channels (Carrascal et al., 2005), other studies have shown a relationship between morphology and membrane properties that can influence electrophysiology (Nunez-Abades and Cameron,

* Corresponding author at: Loma Linda University, Lawrence D. Longo MD Center for Perinatal Biology, 24941 Stewart St., Loma Linda, CA, 92350, USA.
E-mail address: cgwilson@llu.edu (C.G. Wilson).

https://doi.org/10.1016/j.resp.2018.07.009
Received 16 April 2018; Received in revised form 13 July 2018; Accepted 25 July 2018
Available online 26 July 2018

1997). A recent study of XII MNs in mice found changes in dendrite morphology and dendritic spine distribution from embryonic age E18 through postnatal age P28 (Kanjhan et al., 2016). In addition, a few studies have utilized single compartment models (soma) to model various aspects of hypoglossal motoneuron electrophysiology (Fietkiewicz et al., 2011; Purvis and Butera, 2005). However, most studies (morphological or electrophysiological) have examined only a single or small window of ages within the neonatal period, or group ages in a somewhat arbitrary manner (Kanjhan et al., 2016; Nunez-Abades and Cameron, 1995).

Therefore, there is a need to understand both electrophysiological behavior and morphology to assess the relationship between morphology and biophysical function in XII MNs. Previously we have reported on the changes in XII MN morphology with age during the first three weeks post-birth (Williams et al., 2018). In this study we modeled passive and active electrophysiological properties based on actual morphological geometries of XII MNs. Our objective was to simulate actual electrophysiology experiments on morphologically accurate XII MNs reconstructed from Golgi-Cox stained neurons across a range of developmental windows and compare our simulation results with experimental results reported in the literature. We hypothesized that morphological characteristics such as total volume or total surface area can influence the simulated passive and active electrophysiological behavior of hypoglossal motoneurons. We chose three ages ranging from the first, second, and third weeks of development and utilized established single-compartment models and iterated the parameter values until experimental and computational results were comparable. Finally, we examined correlations between the electrophysiology and neuron morphology.

2. Material and methods

2.1. Animals

Pregnant Sprague-Dawley dams (Charles River Laboratories International, Inc., Wilmington, MA) obtained approximately 18 days after the start of pregnancy (embryonic day 18, E18) were allowed to deliver naturally in the Loma Linda University Animal Care Facility. Previously we studied the changes in XII MN morphology at nine postnatal ages (Williams et al., 2018). In this study, we assessed rat pups at three postnatal ages (P3, P10, and P17 days). All procedures and protocols used in this study were approved by the Institutional Animal Care and Use Committee at Loma Linda University and followed the guidelines by the National Institutes of Health *Guide for the Care and Use of Laboratory Animals* (http://www.ncbi.nlm.nih.gov/books/NBK54050).

2.2. Golgi-cox staining

On the appropriate developmental day, animals were weighed, euthanized, and the brain extracted. For postnatal age P3 the pups were anesthetized with isoflurane (Western Medical Supply, Arcadia, CA) until unresponsive to toe pinch, then their brains were rapidly extracted and placed in chilled 0.9% saline. For postnatal ages P10 and P17, animals were placed in an induction chamber with oxygen (100%) flow at 0.65 L/min and isoflurane administered at a concentration of 3 to 4% based on the postnatal age. Once the animal was unresponsive to toe pinch it was removed from the induction chamber, placed on a platform with the oxygen and isoflurane continuously administered via a nose cone, and perfused with 0.9% saline for approximately two minutes after which the brain was removed. For age P3 the whole brain was maintained intact while for P10 and P17 pups the brain was sectioned coronally into two tissue blocks to maintain a more consistent tissue volume.

The brains were immediately transferred from 0.9% saline to impregnation solution from a commercial kit (*superGolgi Kit*, Bioenno Tech, LLC, Santa Ana, California). Sections impregnated at different time durations showed that the best results were obtained with 7 days of impregnation at room temperature changing the solution after the initial two days. Therefore, impregnation solution was changed after two days then the specimens were left in the solution for five more days according to the supplier's instructions and previous reported methods with all steps performed at room temperature (Das et al., 2013). After a total of 7 days in impregnation solutions the brains were placed in two changes of post-impregnation buffer (changed each day for two days). We performed coronal sectioning of tissue at 150 μm with a vibratome (Vibratome Series 1000 Classic–Tissue Sectioning System, Leica, St. Louis, MO) mounting the sections onto gelatin-coated slides and then allowed slides to dry slowly in a humidified chamber overnight (Das et al., 2013; Gibb and Kolb, 1998). The slides were dried at room temperature and humidity for approximately one hour and then rehydrated in phosphate buffered saline, stained, placed in post-staining buffer, and then washed, dehydrated, and cleared in xylene as per the supplier's instructions and the literature (Das et al., 2013). After staining, Permount (Fisher Scientific, SP-15, Waltham, MA) was applied to the slides which were then cover-slipped and allowed to fully dry before subsequent imaging.

2.3. Imaging

The XII nucleus from each animal was identified by comparing brainstem sections imaged using a 2x objective with atlases (Khazipov et al., 2015) corresponding to the appropriate postnatal period. For the P3 animals single image stacks were obtained using a microscope (Zeiss Axio Imager, Carl Zeiss Microscopy, LLC One Corporation Way 1, Peabody, MA) with a motorized stage (Applied Scientific Instrumentation, Eugene, OR) and imaging software (*Stereologer*, Stereology Resource Center, Tampa FL). We used a 40x dry objective (Numerical Aperture = 0.75, Working Distance = 0.17 mm) to acquire image stacks for each XII MN with one image every 2 μm in the z-direction. For the P10 and P17 animals, we acquired single and multiple stacks. Multiple z-stacks were required for many of the P10 and P17 animals in order to image the entire dendritic morphology of a single neuron with a 40x dry objective (Numerical Aperture = 0.95, Working Distance = 0.17 mm), so we used another microscope (Keyence, BZ-9000, Itasca, IL) to image these. This inverted microscope is an integrated system with a motorized stage and software for the acquisition of single or merged multiple images in bright-field or fluorescent modes (https://www.americanlaboratory.com/617-News/19006-BZ-9000-All-in-one-Fluorescence-Microscope/). The Keyence microscope can also generate single stacks or multiple stacks with sufficient overlap to allow for rapid stitching of the acquired z-stacks. This microscope allows large volumes of tissue to be easily imaged as multiple stacks by the user setting three or more points designating the outer boundary to be imaged and then the software calculates the number of stacks by which the entire area is obtained. Both microscope systems utilized software for controlling the motorized stage to obtain images and compensate for optical aberrations due to refraction (Glaser, 1982) and other optical limitations.

2.4. Mapping of neuron locations

The position of each XII MN was measured with *ImageJ* to acquire the length and angle of a line from the apex of the fourth ventricle (rostral) or center of the central canal (caudal). These lengths and angles were converted to x (horizontal) and y (vertical) distances with x representing the medial-lateral and y representing the dorsal-ventral direction. These points were plotted relative to the anatomical reference point along with the boundary of the XII nucleus determined in a similar manner, as previously described (Kanjhan et al., 2016). For the rostral-caudal extent of XII nucleus, sections were matched with a representative rat atlas for each postnatal age and the lambda coordinate along with the y axis (dorsal-ventral direction) was used to

Table 1
List of parameters with their abbreviation (Abbrev), units of measurement, and values for P3, P10, and P17 XII MNs. The initial values were taken from a previously published single-compartment model (Fietkiewicz et al., 2011) and then the values were iterated till they matched previous experimental results (Nunez-Abades et al., 1993). The model parameter which allowed for model results to match experimental results are the values listed in this table.

Parameter	Abbrev	Units	P3	P10/P17
Cytoplasmic resistance	R	Ω-cm	100	100
Membrane Capacitance	C_m	pF/cm^2	0.50	0.25
Passive conductance	$\bar{g}_{pas}$	S/cm^2	2.5×10^{-4}	2.5×10^{-4}
Passive membrane potential	E_{pas}	mV	−70	−70
Leakage conductance	$\bar{g}_{leak}$	S/cm^2	1.25×10^{-4}	1.25×10^{-4}
Leakage membrane potential	E_{leak}	mV	−50	−50
Persistent sodium conductance	$\bar{g}_{Nap}$	S/cm^2	3.975×10^{-5}	3.975×10^{-5}
Fast-transient potassium conductance	$\bar{g}_{A}$	S/cm^2	2.5×10^{-3}	2.5×10^{-3}
Soma				
Fast sodium conductance	$\bar{g}_{Na\ (soma)}$	S/cm^2	7.5×10^{-3}	7.5×10^{-3}
Fast sodium membrane potential	$E_{Na\ (soma)}$	mV	60	60
Potassium conductance	$\bar{g}_{K\ (soma)}$	S/cm^2	3.2×10^{-2}	3.2×10^{-2}
Potassium membrane potential	$E_{K\ (soma)}$	mV	−80	−80
Hyperpolarization-activated conductance	$\bar{g}_{H\ (soma)}$	S/cm^2	2.5×10^{-5}	2.5×10^{-4}
Hyperpolarization-activated membrane potential	$E_{H\ (soma)}$	mV	−38.8	−38.8
Dendrites				
Fast sodium conductance	$\bar{g}_{Na\ (dendrite)}$	S/cm^2	7.5×10^{-4}	7.5×10^{-4}
Fast sodium membrane potential	$E_{Na\ (dendrite)}$	mV	60	60
Potassium conductance	$\bar{g}_{K\ (dendrite)}$	S/cm^2	3.2×10^{-3}	3.2×10^{-3}
Potassium membrane potential	$E_{K\ (dendrite)}$	mV	−80	−80
Hyperpolarization-activated conductance	$\bar{g}_{H\ (dendrite)}$	S/cm^2	2.5×10^{-6}	2.5×10^{-5}
Hyperpolarization-activated membrane potential	$E_{H\ (dendrite)}$	mV	−38.8	−38.8

plot location in the sagittal plane similar to the methods previously described (Kanjhan et al., 2016; Khazipov et al., 2015). Due to size differences between pups at each of the postnatal ages, lambda was normalized to the lambda value at the obex. Neurons located in the XII nucleus for both the coronal and sagittal maps were included while any neurons outside the XII were excluded from analysis.

2.5. Selection of motoneurons

The majority of neurons in the XII nucleus are MNs, yet there are a few interneurons (Boone and Aldes, 1984; Cooper, 1981; Takasu and Hashimoto, 1988). Due to the presences of these interneurons, we needed criteria to determine if the measured neuron was a motoneuron. In the adult rat motoneurons are larger in diameter (19–50 μm) than the interneurons (10–18 μm) (Boone and Aldes, 1984; Cooper, 1981). For mouse XII MNs it has been shown that there is approximately a 25% decrease in major diameter at P1–P4 when compared with P14–P28 (Kanjhan et al., 2016). Adult interneurons have been described as fusiform or oval in shape with few primary dendrites from both poles and from the center, while motoneurons were multipolar in shape (Boone and Aldes, 1984; Takasu and Hashimoto, 1988). However, this has not been as well established for neonatal XII neurons (Kanjhan et al., 2016; Nunez-Abades et al., 1994; Nunez-Abades and Cameron, 1995). Therefore, our main criteria for distinguishing a motoneuron from an interneuron was: at P3 the soma size (diameter) needed to be at least 18 μm and at least 20 μm at P10 and P17. The shape (oval, fusiform, multipolar) of the neuron, as previously described, was then used as a secondary criterion (Boone and Aldes, 1984; Cooper, 1981; Fukunishi et al., 1999; Nunez-Abades et al., 1994; Nunez-Abades and Cameron, 1995; Takasu and Hashimoto, 1988).

2.6. 3D reconstructions

For the P3 animals, single image stacks were obtained due to their relatively compact dendritic arbor, however for the P10 and P17 animals, multiple stacks were stitched together using the *ImageJ* stitching plug-in (Preibisch et al., 2009). From the image stacks, 3D reconstructions were obtained For P3, P10, and P17 XII MNs using *Neuromantic* (Reading, UK) with volume and surface area measured for each neuron (Myatt et al., 2012). For P3, P10, and P17 XII MNs with volumes equaled to or approximating the minimum, maximum, and average volume values for the soma or dendrites were selected. This provided a sample of XII MNs for each of the three ages with ten from P3 and six each for P10 and P17 ages, resulting in a total of 22 neurons for simulation. Minimum, maximum, and average volumes were used to allow for the largest range of morphologies.

2.7. Simulations

Selected neurons were imported into the NEURON simulator and simulations were run using the soma diameter from each reconstructed neuron along with its dendritic tree morphology. A simplified model based on the work of Purvis and Butera (2005) was used and included the following ionic currents: fast-sodium (I_{Na}), persistent sodium (I_{NaP}), fast-transient potassium (I_A), potassium (I_K), hyperpolarization-activated current (I_h), and potassium leakage (I_{leak}) (Engel et al., 1999; Fietkiewicz et al., 2011; Purvis and Butera, 2005). The Hodgkin-Huxley current balance equation for the model is:

$$C_m \frac{dV}{dt} = I_{leak} + I_{NaP} + I_A + I_{Na(soma)} + I_{h(soma)} + I_{K(soma)} + I_{Na(dendrite)} + I_{h(dendrite)} + I_{K(dendrite)}$$

Where V is the membrane potential, t is time, and C_m is the membrane capacitance. For an ionic current I_x, the current is expressed by the equation

$$I_x = \bar{g}_x \cdot y_x \cdot (V - E_x)$$

Where $\bar{g}_x$ is the maximum conductance, y_x is the product of one or more activation or inactivation gating variables raised to integer powers, V is the membrane potential, and E_x is the equilibrium potential. The equations for each y_x were taken from previous work (Fietkiewicz et al., 2011; Purvis and Butera, 2005). The initial values for the parameters were also taken from previous work (Fietkiewicz et al., 2011) and then iterations performed to adjust values until there was a match to published experimental data (Nunez-Abades et al., 1993) resulting in the final parameter values used in the study (Table 1).

Two different experiments were simulated with the model replicating previous electrophysiological data from genioglossal MNs

(Nunez-Abades et al., 1993). We selected one experiment that yielded passive properties from current-voltage plots from current clamp. The experiment and our simulation injected currents from –0.1 to –0.6 nA for P3 XII MNs and from –0.1 to –1 nA for P10 and P17 both in increments of –0.1 nA. The other experiment generated single action potentials yielding active properties including the medium afterhyperpolarization (mAHP) potential (Nunez-Abades et al., 1993; Purvis and Butera, 2005). In the reported experiment, the membrane was held at a fixed potential varying from −50 mV to −85 mV while a current was injected for a duration of 0.1 ms. In our simulation we chose to set the E_{pas} to values of −50, −60, −70, −80, and −85 mV to generate the five values reported in the experiment. The results of the simulation were compared with those previously obtained from Nunez-Abades and colleagues (Nunez-Abades et al., 1993).

2.8. Data analysis

Descriptive summary statistics of simulation results were generated for each of the three ages. Nonparametric statistics were used (Kruskal-Wallis test and Dunn multiple comparisons) to compare measured and simulation results. Correlation coefficients and regression analyses were calculated for the electrophysiological measures as a function of the morphology (volume or surface area). The data was fitted with the equation $Y = a \times X^b$, where 'a' is the intercept and 'b' is the exponent or slope of the curve.

3. Results

3.1. 3D morphometrics and electrophysiology

Examples (based on the average volume for either soma or dendrites) of 3D reconstructions and Sholl profiles for P3, P10, and P17 neurons are shown in Fig. 1. As can be seen from the Sholl profiles, the morphology changes with increases in dendritic tree size and complexity. Specifically, the number of primary branches increased from P3 to P10 but did not change from P10 to P17 (Table 2). The maximum intersections, which indicates the number of dendrites crossing at a specific radius, increased with increasing age, but the ramification index (maximum number of intersections normalized by the number of primary branches) only increased from P10 to P17. The radius at the maximum number of intersections and enclosing radius represents the size of the dendritic tree which increased with increasing age (Table 2). The total volume and total surface area increased with age—with total volume increased from 4766 μm^3 for P3 to 16,904 μm^3 for P17 (a factor of about 3.5) (Table 3) and total surface area increased from 4258 μm^3 at P3 to 13,510 μm^3 at P17 (a factor of about 3.2) (Table 3). Statistically, only the P3 and P17 neurons were significantly different for both volume and surface area ($p < 0.05$). Examples of the simulation output from the current-voltage experiment for the P3, P10, and P17 XII MNs are shown in Fig. 2. It was necessary to decrease the hyperpolarization-activated current (I_h) by a factor of 10 for both soma and dendrites and increase membrane capacitance by a factor of 2 to match the P3 simulation results to the experimental data. Both peak and steady-state resistance decreased with age. From P3 to P17 the peak resistance decreased by 63% while the steady-state decreased by 71%. For the single action potential (Fig. 3) we observed decreasing width in the action potential with increasing age and the mAHP amplitude decreased with increasing membrane potential (Fig. 3). There was no statistically significant change in mAHP amplitude or duration with age (Table 3), but power analysis suggested that, for mAHP amplitude, a

Table 2
Summary statistics of morphological data from 3D Sholl analysis. For each age the mean ± standard deviation is given for each parameter along with the median shown in (). Shown are the number of primary branches, maximum intersection (number of dendrites), radius at which the maximum intersections occur, ramification index (maximum intersections ÷ number of primary branches), and enclosing radius (radius at which last intersection occurs).

Parameter	P3 (N = 10)	P10 (N = 6)	P17 (N = 6)
Number of Primary Branches	3.1 ± 0.9 (3.0)	4.3 ± 1.9 (4.0)	4.0 ± 0.6 (4.0)
Maximum Intersections	6.7 ± 3.9 (6.5)	8.7 ± 2.7 (8.5)	11.7 ± 2.3 (11.5)
Radius at Max Intersections (μm)	36 ± 20 (40)	37 ± 24 (35)	100 ± 59 (95)
Ramification Index	2.2 ± 1.2 (2.0)	2.3 ± 1.2 (2.3)	3.0 ± 0.9 (3.0)
Enclosing Radius (μm)	145 ± 63 (115)	222 ± 76 (220)	302 ± 78 (280)

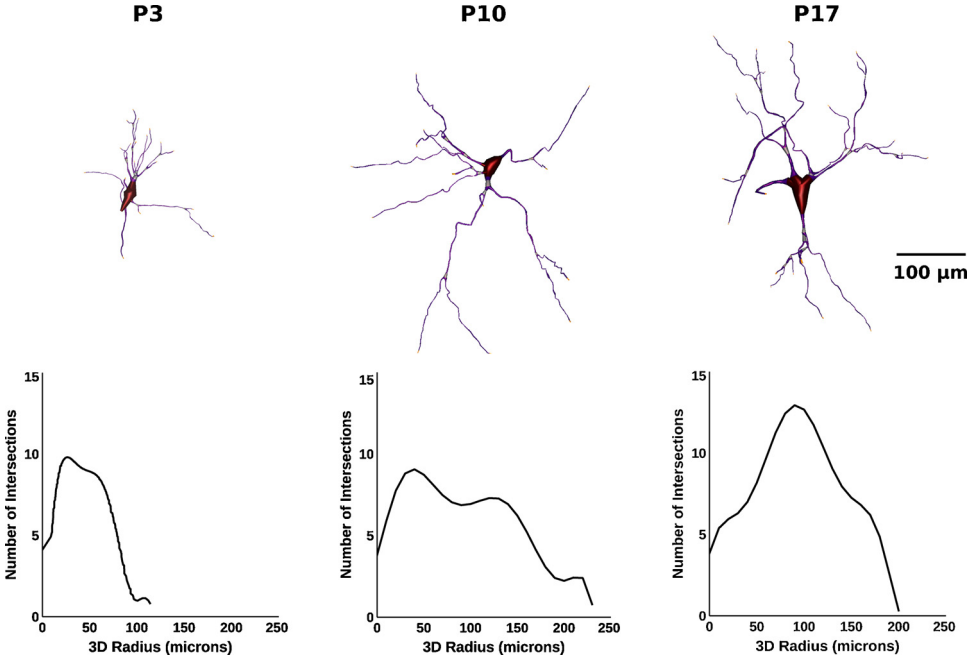

Fig. 1. Morphology of hypoglossal motoneurons at P3, P10, and P17. The 3D reconstructions (top) and their associated Sholl profiles (bottom) are shown.

Table 3
Summary statistics of morphological and biophysical properties from XII MNs. For each age the mean ± standard deviation is given for each parameter along with the median shown in (). Shown are the morphometric parameters (volume and surface area), passive properties (peak and steady-state resistance), and the active properties (amplitude and duration of the medium after-hyperpolarization potential, mAHP).

Parameter	P3 (N = 10)	P10 (N = 6)	P17 (N = 6)
Volume (μm3)	4766 ± 4510 (3334)	7259 ± 6104 (5156)	16,904 ± 6997 (17,390)
Surface Area (μm2)	4258 ± 3759 (3320)	7096 ± 3856 (7112)	13,510 ± 3868 (12,822)
Peak Resistance (MΩ)	143 ± 101 (117)	129 ± 50 (126)	53 ± 36 (52)
Steady-State Resistance (MΩ)	140 ± 101 (114)	102 ± 42 (107)	41 ± 26 (39)
mAHP amplitude (mV)	2.77 ± 0.65 (2.57)	4.61 ± 1.21 (4.57)	3.69 ± 1.35 (3.70)
mAHP duration (ms)	173 ± 37 (183)	205 ± 21 (211)	184 ± 34 (190)

sample size of 75 neurons for each age group would be required to fully assess the mAHP changes.

3.2. Electrophysiology as a function of morphology

The peak resistance (R_{peak}) correlated with the total volume and surface area of the XII MNs (Fig. 4A and B). The intercept of the curve for total volume versus R_{peak} (Fig. 4A) was 2212 with a slope of –0.38 ($R = 0.5462$, $p < 0.01$) while the total surface area versus R_{peak} (Fig. 4B) had an intercept of 8227 with a slope of –0.53 ($R = 0.5831$, $p < 0.01$). Although the amplitude of the mAHP was not found to be strongly correlated ($R = 0.3375$, $p > 0.20$ for P3 and $R = 0.307$, $p > 0.20$ for P10/P17) with neuron morphology (Fig. 4C), there was a correlation between R_{peak} and the amplitude of the mAHP (Fig. 4D) only for P10 & P17. For the P3 XII MNs the intercept for R_{peak} versus the amplitude of the mAHP was 1.43 with a slope of 0.13 ($R = 0.4058$. $P > 0.10$) and for P10/P17 the intercept was 1.15 with a slope of 0.29 ($R = 0.6796$, $p < 0.01$).

4. Discussion

In this study we have, for the first time, examined the potential relationship between the electrophysiological behavior and the morphology of developing XII MNs. We simulated electrophysiology behavior based on 3D morphology measured from XII MNs in a rat pup model comparing theoretical passive and active electrophysiology properties with previously reported experimental results (Nunez-Abades et al., 1993). While many conductances play a role in shaping electrophysiological behavior of motoneurons, medium-duration after-hyperpolarization (mAHP) plays a key role in modulating XII MN excitability (Purvis and Butera, 2005). We did not observe a direct relationship between the morphology of the neuron and amplitude of the mAHP, but we did show that mAHP amplitude is dependent on the neuron's passive properties, suggesting an indirect relationship between morphology and active cellular properties. Although there are other studies of hypoglossal motoneuron electrophysiology (Bayliss et al., 1994; Lamanauskas and Nistri, 2008; Lape and Nistri, 2001; Powers and Binder, 2003), most studied specific ion currents. Simulating XII MNs and comparing these studies to experimental data can provide insight into the ion currents but does not provide information on morphology or differences in ion currents between soma and dendrites. Additionally, previous studies have not examined a wide range of longitudinal ages. An exception is the work of Nunez-Abades et al. (1993) who examined P1–P2, P5–P6, P13–P15, and P19–P30 rat pups and we have used their experimental data as a reference for the model reported here. The action potentials and mAHP amplitudes obtained in our models where similar to those in the literature (Nunez-Abades et al., 1993). To match waveforms from published experimental results (Nunez-Abades et al., 1993), we found that the P3 XII MN parameters required more substantive changes in the model than P10 and P17 XII MNs. We were able to demonstrate a relationship between neuron size (volume and surface area) and the passive electrophysiological properties showing decreased resistance (from I to V curves) with increased cell size.

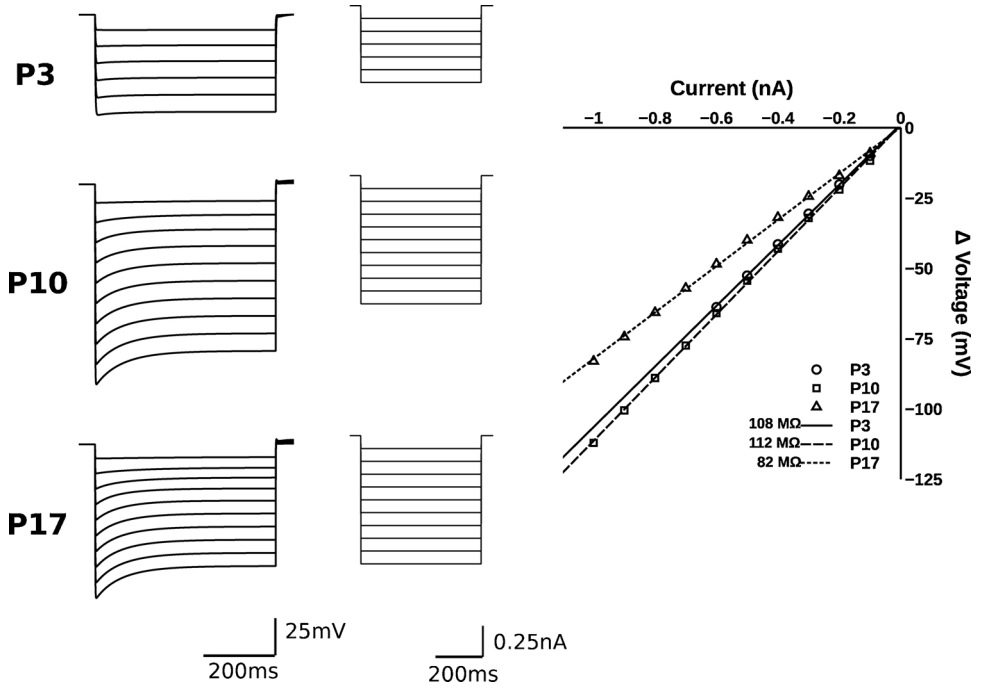

Fig. 2. The I–V curves from P3, P10, and P17 XII MNs. On the left side are the voltage curves corresponding to the injected current (right side) and on the far right is the current-voltage (I–V) curves for the three age groups showing the slopes (resistance).

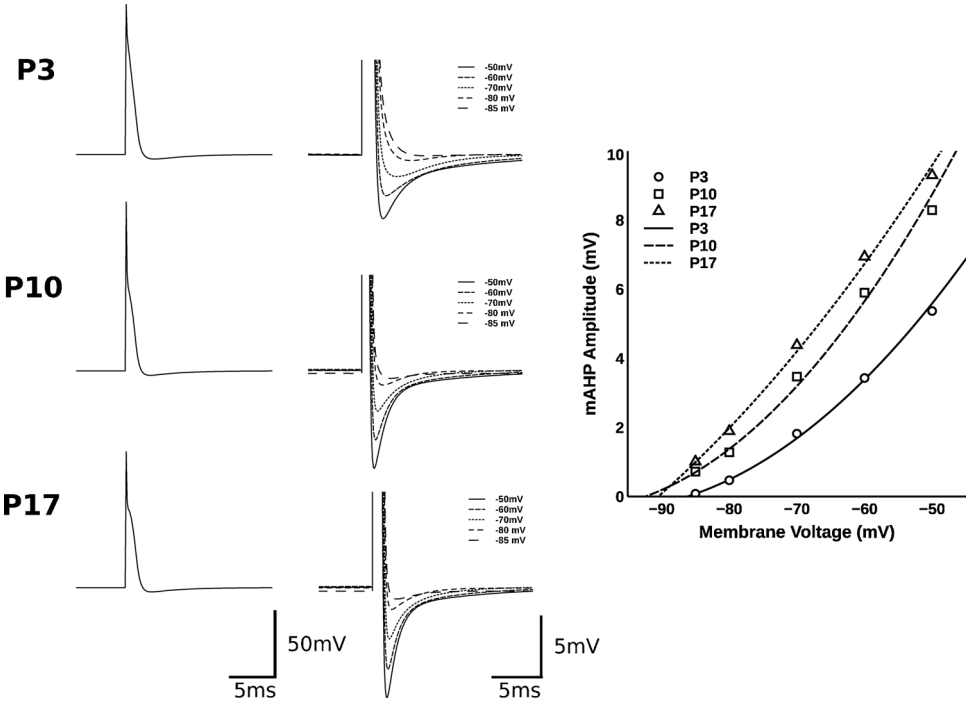

Fig. 3. Action potentials and mAHP from P3, P10, and P17 XII MNs. On the left are the action potentials with expanded views (right) showing the mAHP potentials at each of the membrane potentials. On the far right is a graph of the membrane potential versus the mAHP amplitude for each of the three postnatal ages.

4.1. Morphology

It has been previously shown that certain aspects of XII MN morphology are age dependent and change during development (Kanjhan et al., 2016; Nunez-Abades et al., 1994; Nunez-Abades and Cameron, 1995; Williams et al., 2018). Although a previous study on rat XII MN morphology suggested that soma size changes little with age (Nunez-Abades et al., 1994; Nunez-Abades and Cameron, 1995), more recent studies on mice and rat XII MN morphology have shown that soma size increases with age (Kanjhan et al., 2016; Williams et al., 2018). We

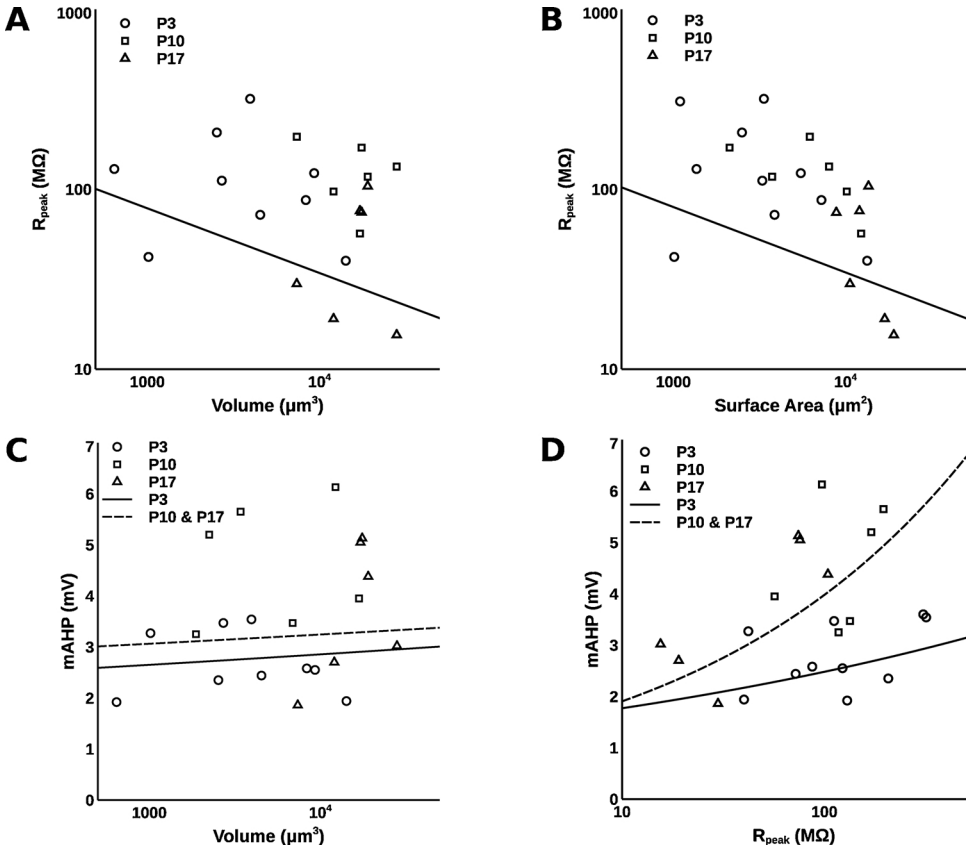

Fig. 4. Regression analysis of passive and active biophysical properties of XII MNs as a function of morphology. Shown are a) total neuron volume versus peak resistance (Rpeak) with regression line for P3, P10, and P17 combined, b) total neuron surface area versus Rpeak with regression line for P3, P10, and P17 combined, c) total neuron volume versus mAHP amplitude with regression for P3 only and regression for P10 and P17 combined, and d) Rpeak versus mAHP amplitude with regression for P3 only and regression for P10 and P17 combined. All regression values are reported in the text.

have previously shown that XII MN morphology can be divided into three developmental windows: P1–P5, P7–P12, and P13–P21. Due to this and the specific ages used in the published experiments (Nunez-Abades et al., 1993) we chose P3, P10, and P17 as representative developmental age groups for this study. Nunez-Abades et al. (1994) reported an increase in terminal branches at P13–P15 with a subsequent decrease at P19–P30. Since our previous study did not examine morphology between P13 and P17, we cannot address this particular group from Nunez-Abades et al. (1994). Also, since we observed dendritic spines, but did not perform measurementsin our previous study, we cannot address the relocation of MN spines reported by Kanjhan et al. (2016). However, we reported that there were changes specific to P7–P12 with the number of primary branches increasing at P7–P12, but we saw no further increase at P13–P21 (Williams et al., 2018), similar to our observations in this study. The changes we saw in this study concerning primary branches, maximum intersections, and ramification index are similar to those we found previously (Williams et al., 2018), but have not been reported elsewhere.

4.2. Electrophysiology

Although the model we used (Fietkiewicz et al., 2011) has a single soma compartment, we incorporated dendrites into our model using the tools provided in NEURON (Fietkiewicz et al., 2011; Purvis and Butera, 2005). In our model, we utilized different values of fast sodium and potassium conductance for soma and dendrites with the dendrite Na^+ and K^+ conductances set 10-fold lower than the soma, and the hyperpolarization-activated current 10-fold lower for dendrites than for soma (see Table 1). A previous model, which included three dendrites with the soma, also used different values for conductance of specific channels (Engel et al., 1999). In this study, we found that the passive and active properties used for postnatal day 3 (P3) in our model did not match previously reported experimental results unless the value for the hyperpolarization-activated current was 10 times less and membrane capacitance twice the value of that used for P10 and P17 neurons. Purvis and Butera (2005) have suggested that the hyperpolarization-activated current is lower in neonates based on differences in mAHP duration between adults and neonates with approximately a ten-fold decrease in neonates compared with adults. Experimental data on membrane properties and cell size suggest that the membrane capacitance can decrease by 50% from P1–P2 to P19–P30 (Nunez-Abades and Cameron, 1997) meaning that the value at P3 is not necessarily the same at P10 or P17. This may also be true for P10 neurons since the membrane properties appear to change with age—and thus likely morphology (Nunez-Abades and Cameron, 1997), and the mAHP changes with age related to the hyperpolarization-activated current (Berger et al., 1996; Cameron and Nunez-Abades, 2000; Purvis and Butera, 2005; Yoshimoto et al., 2015). One study has shown that the electrophysiological properties of P10 XII MNs differ from P17 XII MNs (Nguyen et al., 2004). As a result, the electrophysiological properties of the P10 XII MNs we report here may be different from those seen experimentally, but the previous study we used for comparison did not measure P10 XII MNs (Nunez-Abades et al., 1993) so this is, as of yet, unknown. Therefore, the changes we made to the P3 model are supported by prior experimental work, but further research is required to quantify the electrophysiology changes seen during development.

4.3. Electrophysiology as a function of morphology

We found that the peak resistance correlated with both the total volume and total surface area of the neuron. This has been previously demonstrated experimentally (Nunez-Abades and Cameron, 1997), however we have shown that the proportion of a subset of modeled ionic conductances are different between the P3, P10, and P17 neurons. The membrane resistance (R_M) decreases with increasing age while the amplitude of the mAHP changes little and there is some change in mAHP duration with age. Although the amplitude of the mAHP did not correlate with the volume or surface area of the neuron, we saw a relationship between mAHP amplitude and resistance. Therefore, while morphology may not directly influence the active properties of the neuron, it certainly indirectly affects excitability via the changes we see in the cell's passive properties. Thus, our model provides a more rigorous foundation for understanding how the developmental changes in brainstem neurons can contribute to changes in excitability and reliability of neural activity in hypoglossal motor neurons and provides a starting point for understanding how network properties are altered during development.

4.4. Comparison with previous studies

Although this study is the first to relate biophysical properties and morphology in an extensive sample of developing brainstem neurons, there are theoretical models and experimental studies that have focused on XII MNs. Our model is an extension of two previous models for XII MNs that were single compartment Hodgkin-Huxley style models (Fietkiewicz et al., 2011; Purvis and Butera, 2005). One main difference in our study was the use of morphological data from Golgi-Cox stained XII MNs to inform simulation experiments based on electrophysiological studies published by others (Nunez-Abades et al., 1993). We then compared our simulated results with previously published experimental results from XII MNs at different ages. Although one other study modeled a soma with three non-branching dendrites (Engel et al., 1999), our study used neurons of different sizes, dendrite lengths, and degree of branching. An electrophysiology study on rat vibrissae motoneurons measured active and passive membrane properties as well as measuring neuron morphology (Nguyen et al., 2004). They showed differences in branch length and membrane impedance between P4–P5 and P15–P23 neurons but did not show correlations between the membrane properties and neuron morphology. So, our model incorporates a more extensive set of morphological, electrophysiological, and developmental data to provide a more realistic computational model of the XII MN and a foundation for more realistic neural network models of the brainstem respiratory control circuitry.

4.5. Limitations of model

Although another study (Nunez-Abades et al., 1994) reported > 50% shrinkage in the z-axis, we did not observe any obvious shrinkage in our sections based on stacks of approximately 100 µm without inclusion of the rostro-caudal cut faces of each slice (damaged by the vibratome blade). There are obvious differences including differences in slice thickness—the study by Nunez-Abades et al., (1994) used 300 µm thick sections while we used 150 µm thick sections. When processing brain tissue section mounting, embedding the tissue, and dehydration can result in tissue shrinkage (Andersen and Gundersen, 1999; Reihlen et al., 1994), but the shrinkage can be method dependent (Andersen and Gundersen, 1999; von Bartheld, 2012). Nunez-Abades et al, (1994) performed iontophoretic injections of neurobiotin followed by fixation with 4% PFA while we processed fresh tissue blocks sectioning later without embedding the tissue. We dehydrated the sections during the staining process, but this was after impregnation of the tissue which may reduce shrinkage (Gibb and Kolb, 1998). In addition to shrinkage related to tissue processing, there is the issue of sampling from our previous study (Williams et al., 2018). Instead of sampling based on variance, we could have used random sampling from the broader number of neurons we stained, however, we chose not to randomize the sub-set of neurons we assessed in this study for two reasons. First, in our previous study we found that the morphological data was not normally distributed for most of the parameters we quantified, and many were best represented by the sum of two normal distributions (Williams et al., 2018), which may not be well represented with random sampling unless the sample size is sufficiently large (Finch et al., 1997; Green,

1991; Kelley, 2005). Second, our primary focus was the possible correlation and relationship between morphology and electrophysiology. The size effect for regression includes the slope and variances for the x and y axes, but we did not know what the slope value would be, and we were using a power function for the regression equation. So, this complicates selection of representative neurons by strictly random sampling. To obviate this problem, we will develop computer models of a larger range of neurons in future studies with the goal of more complete characterization of developing XII MNs.

Our model was limited by gaps in our knowledge concerning the range of ionic conductances expressed and present in the membrane of XII MNs as well as differences in channel density on dendrites and the soma and detailed understanding of how those changes occur across the time course of early development. Other studies have established the location of some voltage-gated ion channels (Vacher et al., 2008), but little is known about which ion channels are expressed and where changes in expression occur for XII MNs. There are many studies of voltage-gated ion channel function (Ekberg and Adams, 2006; Jan and Jan, 2012; Johnston et al., 2010; Yu and Catterall, 2003) and XII MNs specifically (Bayliss et al., 1994; Lape and Nistri, 2001; Powers et al., 1999; Powers and Binder, 2003), but there is no comprehensive information about ion channel relative densities on soma and dendrites in XII MNs. One study found that ion channel expression in the rat ventral respiratory column varies between adult and neonates with a subset of sodium, potassium, and calcium channels having a six-fold or more increase in adults when compared to neonates (González-Castillo et al., 2017). However, in our study, we found that the surface area in P17 neurons was about 3-fold greater compared with P3 neurons, suggesting that the density may only have about a 2-fold or more increase in our models. The different sub-types of voltage-gated ion channels and which are present on the somata and dendrites of XII MNs is another factor having a profound effect on electrophysiological behavior. Beckh and colleagues showed that from P1 to about P10 sodium channel III (Na_v 1.3) is expressed on neurons while sodium channel I (Na_v 1.1) is expressed from P10 through adults (Beckh et al., 1989). These two sodium channel sub-types (Na_v 1.1 and Na_v 1.3) exhibit different activation, inactivation, and deactivation kinetics (Ekberg and Adams, 2006; Vacher et al., 2008). Although there are studies of expression of various channels (Beckh et al., 1989; González-Castillo et al., 2017), most are for the whole brain and very few, if any studies of channel distribution on neurons are available for brainstem neurons and less for XII MNs. Consequently, these gaps limit our ability to comprehensively characterize the influence of ion channel type and distribution on the electrophysiological properties of developing XII MNs.

4.6. Future directions

Major challenges in this study included our assumptions about channel location and density in the soma and dendrites. Studies employing immunohistochemistry to stain various channels, allowing quantification of numbers and location/density for XII MNs would aid in model development (Bocksteins et al., 2012) and these studies would be a fruitful avenue for future investigation. Although experimental electrophysiology on XII MNs using neurobiotin/biocytin fills have provided morphology in XII MNs, (Nguyen et al., 2004; Nunez-Abades and Cameron, 1997), there are few studies incorporating both electrophysiology and morphology for the same neuron and a large number of neurons at multiple ages. Combining electrophysiology and morphology data with modeling based on the realistic morphology should provide detailed information about the relationship between morphology and biophysical properties in vitro. This information will provide a better understanding of electrophysiological behavior as more detailed and extensive computational models are developed for motor systems as well as higher CNS neural networks.

4.7. Conclusions

The results from this study suggests that the passive properties (resistance and capacitance) correlate with the developmental morphology changes in hypoglossal neurons. Although the active properties were not found to correlate significantly with morphology—particularly the amplitude of mAHP—more work must be done to address this feature of XII MN modeling. Our modeling results and comparison with experimental data reported in published literature suggest that the ion currents are changing with age—resulting in changes of both the passive and active properties. However, very few studies have thoroughly studied the electrophysiology of developing neurons in functional motor networks. Our work provides a foundation for more realistic neuron simulations being incorporated into computational models of the respiratory neural network in the mammalian brainstem.

Acknowledgments

Imaging was performed in the LLUSM Advanced Imaging & Microscopy Core with support from NSF grant MRI-DBI 0923559 & LLUSM. The authors thank Johnny Figueroa, PhD for use of the Keyence microscope. Grateful thanks also to Dr. Denise L. Bellinger and Dr. Sean M. Wilson for assistance with the manuscript.

References

Andersen, B.B., Gundersen, H.J., 1999. Pronounced loss of cell nuclei and anisotropic deformation of thick sections. J. Microsc. 196, 69–73.
Bayliss, D.A., Viana, F., Bellingham, M.C., Berger, A.J., 1994. Characteristics and postnatal development of a hyperpolarization-activated inward current in rat hypoglossal motoneurons in vitro. J. Neurophysiol. 71, 119–128.
Beckh, S., Noda, M., Lubbert, H., Numa, S., 1989. Differential regulation of three sodium channel messenger RNAs in the rat central nervous system during development. EMBO J. 8, 3611–3616.
Berger, A.J., Bayliss, D.A., Viana, F., 1996. Development of hypoglossal motoneurons. J. Appl. Physiol. 81, 1039–1048.
Bocksteins, E., Shepherd, A.J., Mohapatra, D.P., Snyders, D.J., 2012. Immunostaining of voltage-gated ion channels in cell lines and neurons – KeyConcepts and potential pitfalls. In: Dehghani, H. (Ed.), Applications of Immunocytochemistry. InTech.
Boone, T.B., Aldes, L.D., 1984. The ultrastructure of two distinct neuron populations in the hypoglossal nucleus of the rat. Exp. Brain Res. 54, 321–326.
Cameron, W.E., Nunez-Abades, P.A., 2000. Physiological changes accompanying anatomical remodeling of mammalian motoneurons during postnatal development. Brain Res. Bull. 53, 523–527.
Carrascal, L., Nieto-Gonzalez, J.L., Cameron, W.E., Torres, B., Nunez-Abades, P.A., 2005. Changes during the postnatal development in physiological and anatomical characteristics of rat motoneurons studied in vitro. Brain Res. Brain Res. Rev. 49, 377–387. https://doi.org/10.1016/j.brainresrev.2005.02.003.
Cooper, M.H., 1981. Neurons of the hypoglossal nucleus of the rat. Otolaryngol. Head. Neck Surg. 89, 10–15. https://doi.org/10.1177/019459988108900103.
Das, G., Reuhl, K., Zhou, R., 2013. The Golgi-Cox method. Methods Mol. Biol. 1018, 313–321. https://doi.org/10.1007/978-1-62703-444-9_29.
Ekberg, J., Adams, D.J., 2006. Neuronal voltage-gated sodium channel subtypes: key roles in inflammatory and neuropathic pain. Int. J. Biochem. Cell Biol. 38, 2005–2010. https://doi.org/10.1016/j.biocel.2006.06.008.
Engel, J., Schultens, H.A., Schild, D., 1999. Small conductance potassium channels cause an activity-dependent spike frequency adaptation and make the transfer function of neurons logarithmic. Biophys. J. 76, 1310–1319. https://doi.org/10.1016/S0006-3495(99)77293-0.
Feldman, J.L., Del Negro, C.A., 2006. Looking for inspiration: new perspectives on respiratory rhythm. Nat. Rev. Neurosci. 7, 232–242. https://doi.org/10.1038/nrn1871.
Feldman, J.L., Smith, J.C., 1995. Neural control of respiratory pattern in mammals: an overview. In: Dempsey, J.A., Pack, A.I. (Eds.), Regulation of Breathing. Marcel-Dekker, New York, N.Y, pp. 39–69.
Feldman, J.L., Del Negro, C.A., Gray, P.A., 2013. Understanding the rhythm of breathing: so near, yet so far. Annu. Rev. Physiol. 75, 423–452. https://doi.org/10.1146/annurev-physiol-040510-130049.
Ferrante, M., Migliore, M., Ascoli, G.A., 2013. Functional impact of dendritic branch-point morphology. J. Neurosci. 33, 2156–2165. https://doi.org/10.1523/JNEUROSCI.3495-12.2013.
Fietkiewicz, C., Loparo, K.A., Wilson, C.G., 2011. Drive latencies in hypoglossal motoneurons indicate developmental change in the brainstem respiratory network. J. Neural Eng. 8. https://doi.org/10.1088/1741-2560/8/6/065011.
Finch, J.F., West, S.G., MacKinnon, D.P., 1997. Effects of sample size and nonnormality on the estimation of mediated effects in latent variable models. Struct. Equ. Model. Multidiscip. J. 4, 87–107. https://doi.org/10.1080/10705519709540063.
Fukunishi, Y., Nagase, Y., Yoshida, A., Moritani, M., Honma, S., Hirose, Y., Shigenaga, Y., 1999. Quantitative analysis of the dendritic architectures of cat hypoglossal

motoneurons stained intracellularly with horseradish peroxidase. J. Comp. Neurol. 405, 345–358.
Gibb, R., Kolb, B., 1998. A method for vibratome sectioning of Golgi-Cox stained whole rat brain. J. Neurosci. Methods 79, 1–4.
Glaser, E.M., 1982. Snell's law: the bane of computer microscopists. J. Neurosci. Methods 5, 201–202.
González-Castillo, C., Muñoz-Ortiz, E., Guzmán-Brambila, C., Rojas-Mayorquín, A.E., Beltran-Parrazal, L., Ortuño-Sahagún, D., Morgado-Valle, C., 2017. Differential expression of ion channels in adult and neonatal rat ventral respiratory column. J. Mol. Neurosci. https://doi.org/10.1007/s12031-017-1001-2.
Green, S.B., 1991. How many subjects does it take to do a regression analysis. Multivar. Behav. Res. 26, 499–510. https://doi.org/10.1207/s15327906mbr2603_7.
Jan, L.Y., Jan, Y.N., 2012. Voltage-gated potassium channels and the diversity of electrical signalling. J. Physiol. (Paris) 590, 2591–2599. https://doi.org/10.1113/jphysiol.2011.224212.
Johnston, J., Forsythe, I.D., Kopp-Scheinpflug, C., 2010. Going native: voltage-gated potassium channels controlling neuronal excitability. J. Physiol. (Paris) 588, 3187–3200. https://doi.org/10.1113/jphysiol.2010.191973.
Kanjhan, R., Fogarty, M.J., Noakes, P.G., Bellingham, M.C., 2016. Developmental changes in the morphology of mouse hypoglossal motor neurons. Brain Struct. Funct. 221, 3755–3786. https://doi.org/10.1007/s00429-015-1130-8.
Kelley, K., 2005. The effects of nonnormal distributions on confidence intervals around the standardized mean difference: bootstrap and parametric confidence intervals. Educ. Psychol. Meas. 65, 51–69. https://doi.org/10.1177/0013164404264850.
Khazipov, R., Zaynutdinova, D., Ogievetsky, E., Valeeva, G., Mitrukhina, O., Manent, J.-B., Represa, A., 2015. Atlas of the postnatal rat brain in stereotaxic coordinates. Front. Neuroanat. 9. https://doi.org/10.3389/fnana.2015.00161.
Komendantov, A.O., Ascoli, G.A., 2009. Dendritic excitability and neuronal morphology as determinants of synaptic efficacy. J. Neurophysiol. 101, 1847–1866. https://doi.org/10.1152/jn.01235.2007.
Lamanauskas, N., Nistri, A., 2008. Riluzole blocks persistent Na+ and Ca2+ currents and modulates release of glutamate via presynaptic NMDA receptors on neonatal rat hypoglossal motoneurons in vitro. Eur. J. Neurosci. 27, 2501–2514. https://doi.org/10.1111/j.1460-9568.2008.06211.x.
Lape, R., Nistri, A., 2001. Characteristics of fast Na(+) current of hypoglossal motoneurons in a rat brainstem slice preparation. Eur. J. Neurosci. 13, 763–772.
Lindsey, B.G., Rybak, I.A., Smith, J.C., 2012. Computational models and emergent properties of respiratory neural networks. Compr. Physiol. 2, 1619–1670. https://doi.org/10.1002/cphy.c110016.
Liu, Q., Lowry, T.F., Wong-Riley, M.T.T., 2006. Postnatal changes in ventilation during normoxia and acute hypoxia in the rat: implication for a sensitive period. J. Physiol. (Paris) 577, 957–970. https://doi.org/10.1113/jphysiol.2006.121970.
McClung, J.R., Goldberg, S.J., 1999. Organization of motoneurons in the dorsal hypoglossal nucleus that innervate the retrusor muscles of the tongue in the rat. Anat. Rec. 254, 222–230.
Mortola, J.P., 1984. Breathing pattern in newborns. J. Appl. Physiol. Respir. Environ. Exerc. Physiol. 56, 1533–1540.
Myatt, D.R., Hadlington, T., Ascoli, G.A., Nasuto, S.J., 2012. Neuromantic - from semi-manual to semi-automatic reconstruction of neuron morphology. Front. Neuroinf. 6, 4. https://doi.org/10.3389/fninf.2012.00004.
Nguyen, Q.T., Wessel, R., Kleinfeld, D., 2004. Developmental regulation of active and passive membrane properties in rat vibrissa motoneurones. J Physiol 556, 203–219. https://doi.org/10.1113/jphysiol.2003.060087.
Nunez-Abades, P.A., Cameron, W.E., 1995. Morphology of developing rat genioglossal motoneurons studied in vitro: relative changes in diameter and surface area of somata and dendrites. J. Comp. Neurol. 353, 129–142. https://doi.org/10.1002/cne.903530112.
Nunez-Abades, P.A., Cameron, W.E., 1997. Relationship between membrane properties and cell size of developing rat genioglossal motoneurons studied in vitro. Neurosci. Lett. 223, 41–44.
Nunez-Abades, P.A., Spielmann, J.M., Barrionuevo, G., Cameron, W.E., 1993. In vitro electrophysiology of developing genioglossal motoneurons in the rat. J. Neurophysiol. 70, 1401–1411.
Nunez-Abades, P.A., He, F., Barrionuevo, G., Cameron, W.E., 1994. Morphology of developing rat genioglossal motoneurons studied in vitro: changes in length, branching pattern, and spatial distribution of dendrites. J. Comp. Neurol. 339, 401–420. https://doi.org/10.1002/cne.903390308.
Powers, R.K., Binder, M.D., 2003. Persistent sodium and calcium currents in rat hypoglossal motoneurons. J. Neurophysiol. 89, 615–624. https://doi.org/10.1152/jn.00241.2002.
Powers, R.K., Sawczuk, A., Musick, J.R., Binder, M.D., 1999. Multiple mechanisms of spike-frequency adaptation in motoneurones. J. Physiol. Paris 93, 101–114.
Preibisch, S., Saalfeld, S., Tomancak, P., 2009. Globally optimal stitching of tiled 3D microscopic image acquisitions. Bioinformatics 25, 1463–1465. https://doi.org/10.1093/bioinformatics/btp184.
Purvis, L.K., Butera, R.J., 2005. Ionic current model of a hypoglossal motoneuron. J. Neurophysiol. 93, 723–733.
Reihlen, A., Weis, S., Obermaier, G., Dahme, E., 1994. Age-dependent changes in the glial cell nests of the canine rhinencephalic allocortex. A morphometric study. Anat. Rec. 238, 415–423. https://doi.org/10.1002/ar.1092380316.
Takasu, N., Hashimoto, P.H., 1988. Morphological identification of an interneuron in the hypoglossal nucleus of the rat: a combined Golgi-electron microscopic study. J. Comp. Neurol. 271, 461–471. https://doi.org/10.1002/cne.902710313.
Vacher, H., Mohapatra, D.P., Trimmer, J.S., 2008. Localization and targeting of voltage-dependent ion channels in mammalian central neurons. Physiol. Rev. 88, 1407–1447. https://doi.org/10.1152/physrev.00002.2008.
von Bartheld, C.S., 2012. Distribution of particles in the Z-axis of tissue sections: relevance for counting methods. Neuroquantology 10, 66–75.
Williams, P., Bellinger, D.L., Wilson, C.G., 2018. Changes in the morphology of hypoglossal motor neurons in the brainstem of developing rats. Anat. Rec.
Yoshimoto, R., Iwasaki, S., Takago, H., Nakajima, T., Sahara, Y., Kitamura, K., 2015. Developmental increase in hyperpolarization-activated current regulates intrinsic firing properties in rat vestibular ganglion cells. Neuroscience 284, 632–642. https://doi.org/10.1016/j.neuroscience.2014.10.034.
Yu, F.H., Catterall, W.A., 2003. Overview of the voltage-gated sodium channel family. Genome Biol. 4, 207.